Acta Crystallographica Section B
Structural Science
ISSN 0108-7681

Specific twin junctions in doped zirconia

F. M. Morales[a,b]*‡ and M. Rühle[a]

[a]Max Planck Institute for Metal Research, Heisenbergstrasse 3, D-70569 Stuttgart, Germany, and [b]Department of Materials Science, Metallurgic Engineering and Inorganic Chemistry, University of Cádiz, 11520 Puerto Real, Spain

‡ Correspondence should be addressed to F. M. Morales to his current e-mail address (fmiguel.morales@uca.es) or address in Spain.

Correspondence e-mail: fmiguel.morales@uca.es

Received 4 May 2006
Accepted 22 May 2006

The effect of different dopant cations on the phase transformations of the initially stabilized supersaturated tetragonal ZrO_2 phase during various heat treatments has been studied. The obtained fraction of monoclinic grains develop twinned structures, but there is still a lack of information about the character of grain boundaries formed in doped monoclinic solid solutions. The inspection of particular selected-area electron diffraction patterns provides an alternative method with respect to high-resolution electron microscopy or electron back-scattered diffraction for characterizing different twin junctions in various doped zirconia systems. The classification of these special twins is based on the coincidence site lattice concept.

1. Introduction

Yttria stabilized zirconia (YZS) is traditionally used as a thermal barrier coating (TBC; Levi, 2004) or as an electrolyte in solid-state fuel cells (Atkinson *et al.*, 2004). Interestingly, ZrO_2 has also been applied as a gate insulator for electronic devices (Javey *et al.*, 2002) and for the thermophotovoltaic conversion of thermal radiation (Torsello *et al.*, 2004) in which Mg, Ce or Ce–Y doping promotes shape-memory effects (Zhang *et al.*, 2006). However, increasing demands for a higher operating temperature require coatings and layers with improved durability, reliability and performance. This has motivated renewed interest in finding alternative materials whose implementation is advantageous, for example, in enabling a new generation of gas turbine engines. Two important groups of candidates for reducing and/or stabilizing the thermal conductivity with respect to conventional YSZ are emerging; one based on pyrochlore zirconates ($R_2Zr_2O_7$; Zinkevich *et al.*, 2005) and the other on the substitution of Y_2O_3 or co-doping of YSZ with rare-earth oxides (REO) (Levi, 2004). In this context, the effect of trivalent dopant cations (R^{3+}) with different ionic radii on the stability of ZrO_2 initially stabilized in its supersaturated tetragonal phase (t') during high-temperature exposure plus cooling has been studied.

A complete microstructural characterization of the specimens studied shows that diverse phase transitions occur. One of these transitions (the tetragonal to monoclinic martensitic irreversible transformation) is controlled by lattice-invariant shears which lead to the formation of structural twins. Little is known about grain boundaries in ZrO_2 because its extremely fine-grained microstructure makes direct experimental studies very difficult. Crystallogeometrical models of grain boundaries in the monoclinic system are also still under development. Greater knowledge of the structure and the energies of grain boundaries would allow enhanced control of the diffusion

doi:10.1107/S0108768106018878

(Gertsman *et al.*, 1997) or fracture (Watanabe, 1994) properties in polycrystalline zirconia and would open up the possibility of non-deleterious reversible martensitic transformations (Bhattacharya *et al.*, 2004). The present work is mainly focused on the study of the appearance of doped monoclinic zirconia grains. In order to characterize twin boundaries in these typically twinned structures, a feasible and fast procedure based on the analysis of selected-area electron diffraction (SAED) is presented. Twin junctions are shown to have specific features depending on the implemented doping scheme.

2. Experimental

The sample doping and processing were as follows:

(i) t'-ZrO_2 powders were prepared by the reverse co-precipitation of precursor powders from mixed solutions containing the required cations (Rebollo *et al.*, 2003). The dopants used were Sc, Yb, Y, Gd, Nd and La, which were selected to have an increasing degree of ionic-ratio misfit with respect to Zr^{4+} (*i.e.* reducing the solubility and thus the stability of the t' solid solution). The $RO_{1.5}$ oxides were added to ZrO_2 at a composition of 7.6 mol%, except Sc (5.1%) and La (17.7%);

(ii) t' pyrolized powders were pressed into cylinders of 7.1 mm in diameter and 15 mm in length;

(iii) these pellets were pre-sintered for 24 h at 1773 K, which allows very dense samples to be obtained;

(iv) heat treatment was subsequently applied at 1673 K for 48 h.

Steps (iii) and (iv) were employed for 3 h heating and 5 h cooling.

Conventional transmission electron microscopy (TEM), high-resolution TEM (HRTEM) and SAED were used to study the crystalline structure of the grains within the samples after the annealing process. Specimens were prepared using mechanical thinning and Ar^+ milling in a Gatan precision ion-polishing system. TEM was carried out in a Jeol 2000FX electron microscope and a Jeol 4000EX was used for HRTEM, while SAED analyses were performed in both microscopes. Electron diffraction patterns based on the dynamical theory were calculated by EMS software (P. H. Jouneau and Pierre Stadelmann, EPFL, Lausanne).

High spatial resolution (< 20 nm) analytical TEM was carried out on three different microscopes: a Jeol 2000FX equipped with an energy-dispersive X-ray (EDX) detector (Si–Li, Vantage, Noran Instruments), a Jeol 4000FX and a Zeiss EM 912 OMEGA, both supplemented by EDX detectors (HPGe, Voyager, Noran Instruments). In combination with the inspection by electron microscopy and electron diffraction many grains in different samples were tested in these three EDX systems and their respective spectra were analyzed by both '*Spectral Display*' and '*Flame*' software. Non-standard quantitative analyses were made by comparing Zr with R associated signals to give access to the local chemical compositions, which consequently helped to better distinguish the phases adopted by each ZrO_2 grain after the promoted t'-phase destabilization.

3. Results and discussion

For every sample studied, a prolonged high-temperature (> 1473 K) sintering and aging process was used to promote the microstructure into its equilibrium two-phase configuration. This leads to an R-depleted tetragonal form whose temperature of transition from tetragonal (t) to monoclinic (m) is above ambient temperature. In these circumstances, depending on the dopant ionic radius, a smaller or larger monoclinic content is created after the local tetragonal to monoclinic transformations. As a summary, for the tested ZrO_2–R_2O_3 binary metastable solutions (R = Sc, Yb, Y, Gd, Nd and La), the propensity for partitioning and the ensuing monoclinic transformation increases with increasing dopant size, except for Sc where the initial structure is already unstable and only the monoclinic phase has been observed. On the other hand, stabilization of the tetragonal phase is optimal for Yb doping where monoclinic grains were rarely found, while larger cations such as Nd and La tend to stabilize a partial or total pyrochlore cubic phase plus the monoclinic phase. Moreover, the smaller the cation, the more solubility is attained in the monoclinic solid solution attending to EDX measurements. A report on the ZrO_2 phase destabilizations observed will be presented elsewhere (Morales *et al.*, 2006), while the present manuscript focuses on the crystallographic characterization of the monoclinic phases observed.

The $t \rightarrow m$-ZrO_2 martensitic transformation upon cooling is well known and leads to a volume increase of 3–4%, and a shear stress of *ca* 15%. This is accompanied by the formation of an acicular and twinned microstructure, and microcracks at the grain boundaries between the often well orientated parent (t) and product (m) grains (Subbaro, 1981; Bocanegra-Bernal & De la Torre, 2002). These features were observed during our TEM investigations. For example, Fig. 1(a) shows a transition between a partially tetragonal–cubic grain ($t + c$), also known as a 'colony' tetragonal matrix structure (Lanteri *et al.*, 1984), and a twinned monoclinic grain in the Y-containing sample. The square regions indicated by dotted lines are a monoclinic grain boundary (GB) and an interphase boundary (IB), showing a variation in contrast because it is becoming a microcrack just in that region. Fig. 1(b) is an HRTEM micrograph showing the IB previously mentioned placed in the region more on the right than in Fig. 1(a). The crack is unfilled, although an amorphous structure is just visible in the IB–crack transition. The micrograph was taken in the [110] zone axis of the tetragonal grain, but in this condition the HRTEM contrast was also obtained for the adjacent monoclinic grain. This observation indicates a perfect orientational relationship between both grains. In fact, the [111] zone axis of the monoclinic grain is reached by a small tilting. In Fig. 1(b), the inset shows SAED patterns at the bottom and top which were registered in the two commented orientations, while the inset in the center is the diffraction of both grains when the (t + c) grain is in the [110] zone axis. In this pattern, the reflection spots are composed of contributions from both adjacent grains. The visible hexagonal symmetry demonstrates that a shared (habit) plane exists between these crystals. Actually, other examples of the perfect orientational relationship between grains of different phases were found. The fact that the orientation relationships and the presence of habit planes occurs more is another indication of the occurrence of martensitic transformations.

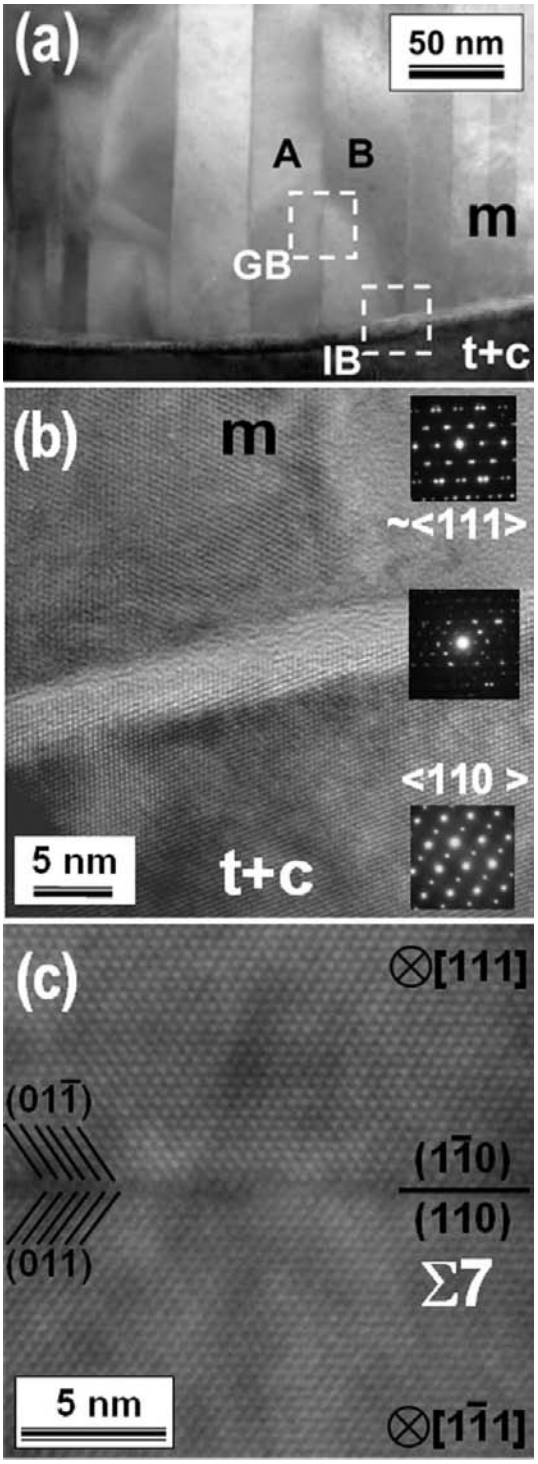

Figure 1
Interface boundary and grain boundary in Y-doped ZrO_2. (*a*) Monoclinic tetragonal IBs are typical in ZrO_2 martensitic transitions. (*b*) Microcracks at the IB often accompany these phenomena, while SAED and HRTEM indicate the existence of habit planes between both grains. (*c*) HRTEM micrographs of the GBs indicate Σ7 consecutive twin junctions in the monoclinic grain.

Fig. 1(*c*) shows the HRTEM micrograph of the region labelled GB in Fig. 1(*a*), but rotated 90° clockwise. This GB of the twinned monoclinic structure is characterized by a (110) twin plane, or more specifically a sigma-7 (Σ7) twin junction. This means that starting from the boundary, advancing towards both perpendicular directions, after 7 times the (110) interplanar distance, the arrangement of the network *(i.e.* atomic positions) is again repeated. This reasoning is the basis for 'exact' or 'near' Coincidence Site Lattice (CSL) models which predict the existence of a low-energy boundary (perfect atomic fit) between crystals oriented in such a way that their infinite lattices have a subset of coincident points. This model is a perfect approach and a tool which has been extensively used for a more complete determination and description of twinned grain boundaries (Grimmer, 1976). However, there is no general method for determining the CSL for the majority of crystallographic systems. For example, for monoclinic ZrO_2, mainly HRTEM (Gertsman, 1999; Gertsman *et al.*, 1999) experiments were devoted to this purpose, whilst the expected or already characterized habit planes or twin junctions might be confirmed by computational calculations (Gertsman *et al.*, 1996; Simha, 1997). Additionally, the distribution of internal interfaces in polycrystals can be revealed by electron backscattered diffraction (EBDS) in combination with scanning electron microscopy (Rohrer *et al.*, 2004; Kim *et al.*, 2006).

In the course of the current investigations, SAED patterns were taken from regions located in the twinned areas of differently doped *m*-ZrO_2 grains. When the twin plane is parallel to the beam of electrons, these patterns show the actual features of grain boundaries in which their misorientations and lattice coincidences can be extracted (Williams & Carter, 1996). This method, quite common for cubic systems, is not widespread for monoclinic networks. We want to emphasize that the use of electron diffraction techniques is appropriate and suitable for the determination of the twin near-CSL character, if appropriate areas and orientations are chosen. Therefore, these SAED patterns are characterized by the superposition of rows of reflections associated with the orientations of the crystals placed on opposite sides of the twin junctions in a twinned area. The problem is then simplified to one of determining and indexing one of the reciprocal networks on the experimental pattern, since the other lattice is obtained if a reflection symmetry operation is applied using the row of reflections associated with the twin plane as a mirror plane.

To illustrate the equivalence between HRTEM and SAED studies of twins, Fig. 2(*a*) shows the fast Fourier transform (FFT) spectra for every side (*A* and *B*) and both sides (*A* + *B*) of the HRTEM micrograph (Fig. 1*c*). Since the FFT spectra of atomic contrast images are equivalent to the diffraction patterns (both give information related to the reciprocal space), reflections associated with the families of the lattice planes on every side (in the [111] and [$1\bar{1}1$] zone axes) appear and are labelled in the $A + B$ FFT spectra of the whole micrograph. Fig. 2(*b*) shows the calculated diffraction pattern of *m*-ZrO$_2$ in the [$1\bar{1}1$] zone axis, where 1, 2 and 3 are the reflections 011, $\bar{1}01$ and 110. The equivalent [111] simulated pattern can be obtained if the same image is flipped vertically. When both simulated patterns are overlapped, making the spots coincident in the central row of the {*nn*0} reflections, after seven parallel rows of reflections in the up and down perpendicular directions, a similar coincidence or matching occurs among the diffraction spots of both lattices. This is illustrated in Fig. 2(*c*) and is further proof of the occurrence of a $\Sigma7$ twin boundary. Thus, the GB can be named as $\langle111\rangle$ $\{011\}\Sigma7$, making reference to the orientation, the twin plane and near CSL character of the twin junction, respectively. Moreover, this notation will be used in the latter discussion for designating *n*-CSL twin boundaries. Fig. 3 shows an experimental SAED pattern of the twinned region presented in Fig. 1(*a*), where the selected area is around 1 µm in diameter. The two coexisting reciprocal networks are represented in part of the same SAED pattern, where the contrast is inverted for clarity. Note that starting from the central row, where the diffracted beam is placed, the arrangement is repeated after seven parallel rows of reflections, as was expected from the previous diffraction simulations. This fact confirms the $\Sigma7$ nature of consecutive twin junctions and exemplifies the general method used to characterize *n*-CSL modes of twins.

Different twins were characterized for the same Y-containing sample. Fig. 4 displays a SAED pattern collected from another monoclinic region, also occurring in a tetragonal contiguous grain. The area indicated by dotted lines is magnified and presented with inverted contrast in the center

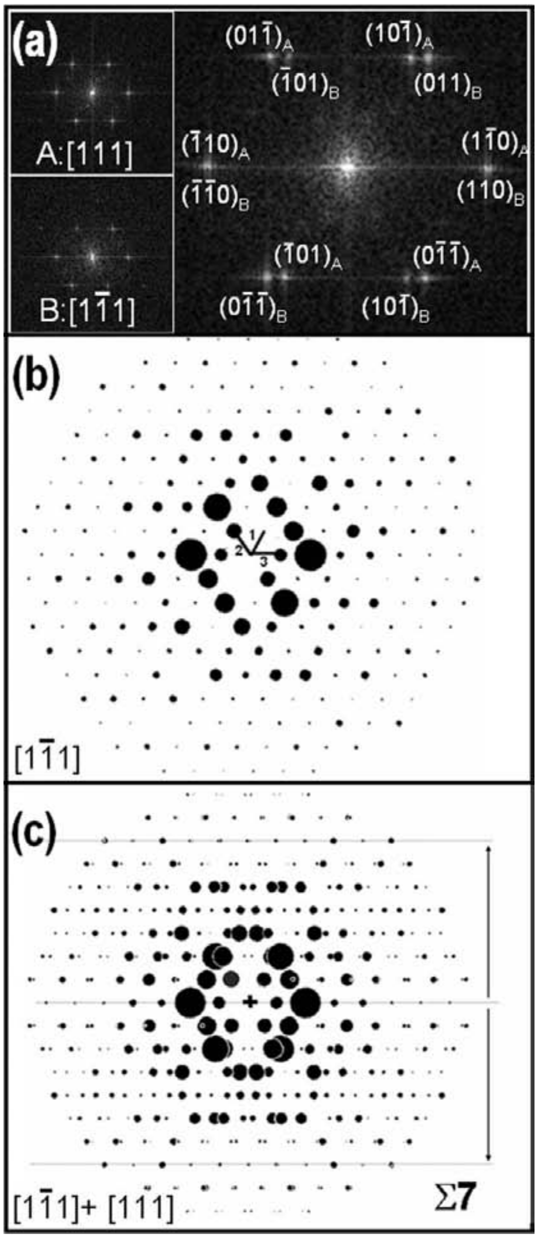

Figure 2
Correspondence between the characterization of CSL twins by HRTEM and SAED. The example stands for the $\Sigma7$ twin between lamellae *A* and *B* shown in Fig. 1. (*a*) FFT spectra of the high-resolution image and (*b*) the calculated diffraction patterns for individual *A* or *B* lath structures (1, 2 and 3 are 011, $\bar{1}01$ and 110 reflections, respectively) display the same features after (*c*) $A + B$ diffraction overlapping. Note that the calculated overlapping diffraction patterns corresponding to *A* and *B* lamellae are similar to the resulting SAED patterns of the whole monoclinic area.

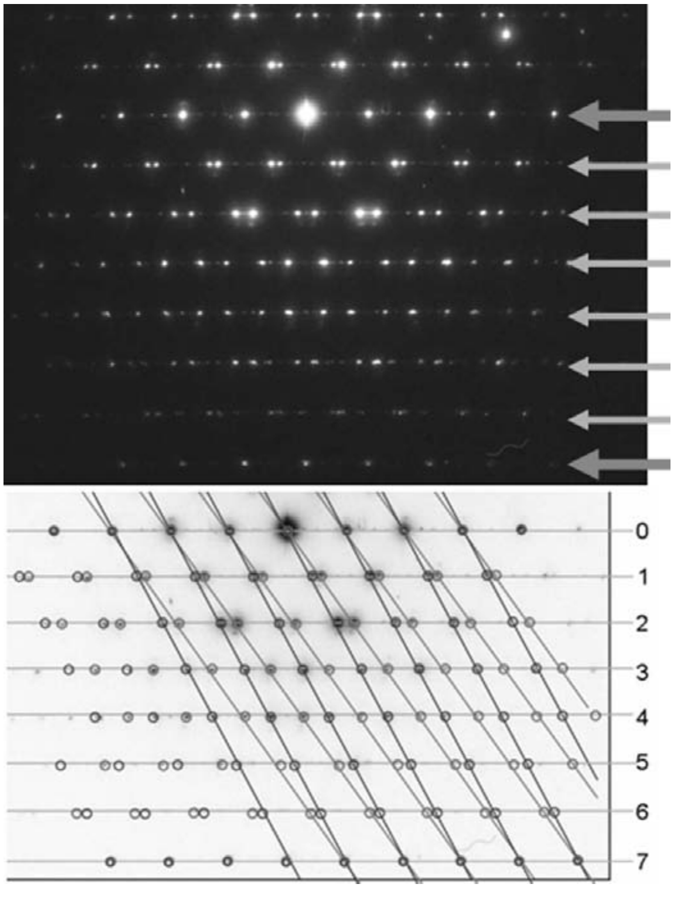

Figure 3
Experimental SAED pattern (top) and associated reciprocal networks (bottom) of *m*-ZrO$_2$ laths at consecutive sides of the $\Sigma7$ twin planes. The coincidence between reflection spots is visible every seven horizontal rows.

of Fig. 4. This pattern exhibits three overlapped networks and therefore the calculated diffraction patterns for the three indexed crystal orientations are shown at the bottom (90° anticlockwise). In this case, the twin junction is catalogued as ⟨011⟩ {100}Σ3, in accordance with the matching between the two families of monoclinic reflections surrounded by grey circles in the SAED pattern and arrows (grey tones) in the expanded insert. Note that after three spacings to the right and to the left of the central line of the overlapped reflections, the spots in the rows coincide again. Also, the tetragonal network (reflections surrounded by white diamonds and indicated with white arrows in the detailed view) is coherent with the twinned crystals. Consequently, there is a total coincidence in the central row of 100 reflections of the twinned crystals in [011] and [$0\overline{1}1$] zone axes, and the 010 reflection of the tetragonal crystal in [101] zone axis, thus indicating the continuity between (100) planes of the monoclinic grains and the (010) tetragonal planes. This also indicates the perfect orientation relationship in the IB between both phases. The orientation of the axis of the zirconia unit cell in the promoted tetragonal to monoclinic phase transformation remains coherent and constant while the cooling-down process takes place.

The sample doped with Sc showed relatively large monoclinic grains (~ 3 μm), as shown in the bright-field (BF) TEM image of Fig. 5(*a*). The lamellar structure is mainly formed by parallel laths and also presents some dislocations and smaller oblique laths (black arrows). When electron diffraction patterns are collected from the region encircled by the white dashed circle, the three laths labelled as *A*, *B* and *C* together originate from the SAED patterns, as presented in Fig. 5(*b*). The pattern is composed of the diffraction associated with monoclinic structures in [001]:*A*, [010]:*B* and [$0\overline{1}0$]:*C* zone axes. This observation was also confirmed by comparing this with other SAED patterns registered for each individual lath. In this way, the twin between *B* and *C* is deduced to be ⟨010⟩ (001) Σ3; taking into account the *n*-CSL model. Reciprocal unit cells for *A*, *B* and *C* are represented in the detail of the SAED pattern in Fig. 5(*c*). The GB between *A* and *B* is also coherent and the continuity between (010) planes of *A* and (001) planes of *B* can be deduced from the overlapping of reflections in the central row. Furthermore, the same arrangement was observed in the sample doped with Yb, *i.e.* three connected monoclinic laths with a ⟨010⟩ (001) Σ3 twin

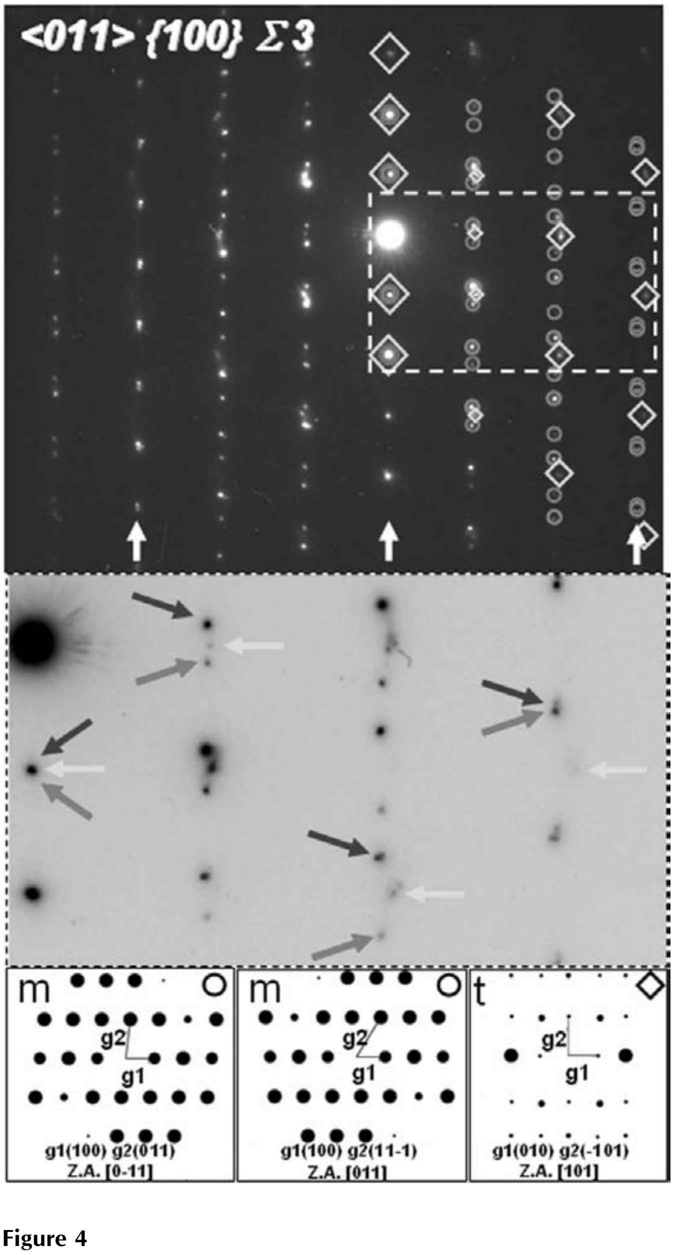

Figure 4
SAED pattern associated with a monoclinic ⟨011⟩ {100} Σ3 twin plus a ⟨101⟩ tetragonal joined crystal in the ZrO_2 sample containing Yttrium. (*a*) The three reciprocal networks are identified in grey for both monoclinic grains and in white for the tetragonal one. (*b*) The image in the center is the detail of the region framed with a dashed line for the corresponding reflections arrowed with the same colours. (*c*) The three indexed and calculated diffraction patterns are shown at the bottom (tilted 90° anticlockwise).

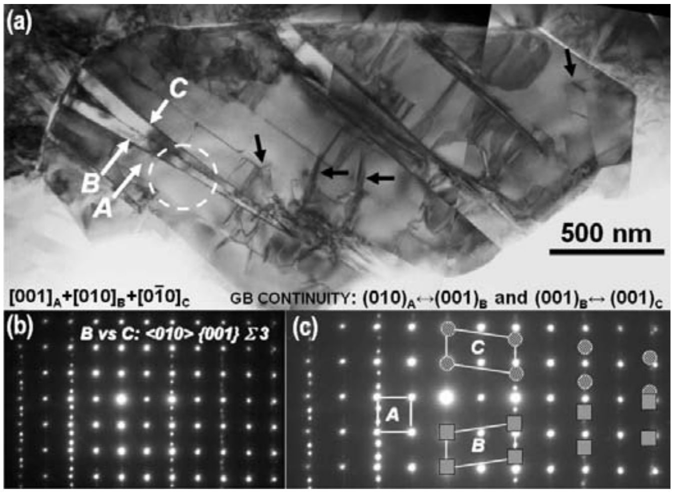

Figure 5
TEM of a monoclinic grain in the sample doped with Sc. (*a*) The three laths labelled as *A*, *B* and *C* present GBs characterized by the continuity between (010) and (001) planes of *A* and *B* and a ⟨010⟩ (001) Σ3 twin between *B* and *C*. (*b*) The SAED pattern shows reflections for *A*, *B* and *C* in [001], [010], [$0\overline{1}0$] orientations, respectively. (*c*) The unit cell for every reciprocal network is shown in the detail of the experimental pattern.

junction between two of them and a continuity of the m-$\mathrm{ZrO_2}$ (010)–(001) planes in the GB with the following lath.

Fig. 6 shows the details of SAED patterns registered in three different regions from another Sc-doped monoclinic grain along with the BF micrograph of this grain. Regions *A* and *B* promote similar SAED patterns, thus having the same ⟨011⟩ {100} Σ3 twin junctions, while region C has a ⟨110⟩ {110} Σ6 twin boundary. Note that the SAED patterns labeled as *A* and *B* are equivalent and that pattern *B* is similar to that squared area in pattern *A*. Similarly, the sample with Nd shows ⟨011⟩ {100} Σ3 twins as those already presented for the Y- and Sc-doped samples. For the SAED pattern from region *C*, a definite SAED area is also magnified and the spots associated with the twinned crystal in the [1$\bar{1}$ orientation are encircled for a clearer visualization of the coincidence after six spacings. For clarification, the BF micrograph of the grain was taken when region *A* was orientated in the ⟨011⟩ zone axis and hence it shows a darker contrast.

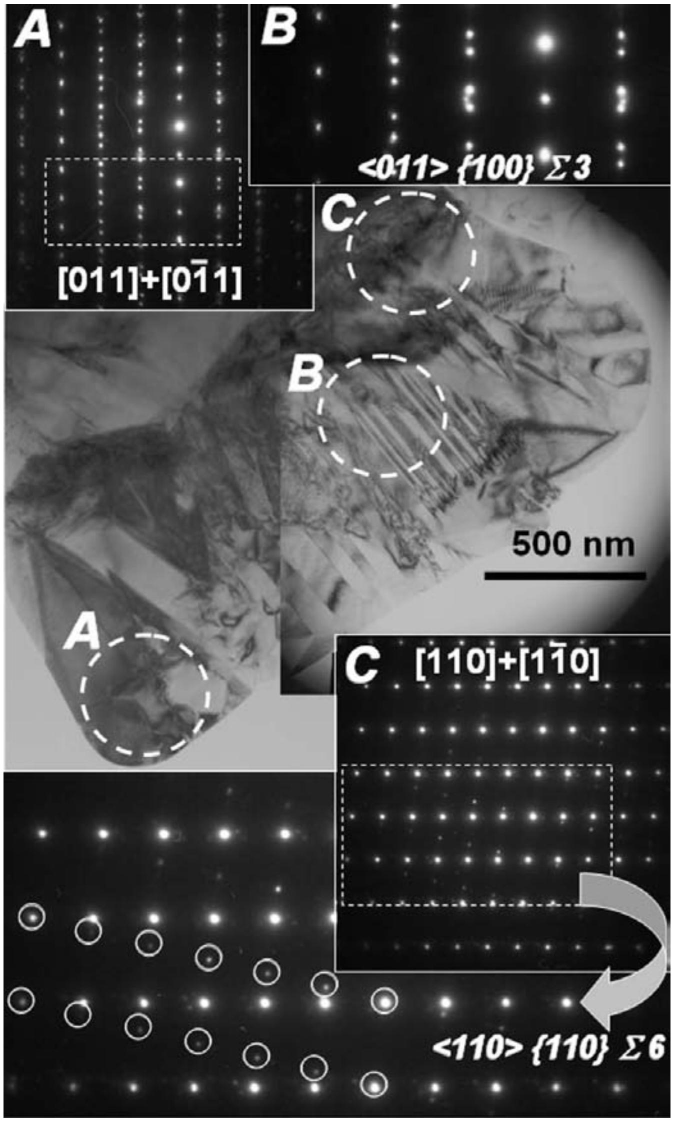

Figure 6
BF-TEM micrograph and corresponding SAED patterns for the regions labelled as *A*, *B* and *C* in a monoclinic Sc-doped $\mathrm{ZrO_2}$ grain. Regions *A* and *B* exhibit ⟨011⟩ {100} Σ3 twin features, while *C* shows a ⟨110⟩ {110} Σ6 twin boundary.

For the La-containing monoclinic grains, a ⟨111⟩ {$\bar{1}$01} Σ6 twin junction was found. Fig. 7(*a*) shows the experimental SAED pattern with the contrast inverted to correspond to the GB previously mentioned. The calculated diffraction pattern for the [1$\bar{1}$1] zone axis is presented in Fig. 7(*b*), where 1, 2 and 3 refer to the 110, 011 and $\bar{1}$01 reflections, respectively. The calculated pattern for the [111] plus overlapping [1$\bar{1}$1] zone axes (Fig. 7*c*) corresponds to the experimental SAED pattern. Other nearby laths contributed to the pattern formation, but after indexing the two main reciprocal networks, the coincidence after the sixth horizontal line parallel to the central row is clearly visible (black arrows in Figs. 7*a* and *c*), indicating the Σ6 character of the twin junction.

The observed twin junctions are summarized in Table 1. The characterized Σ3 twin boundaries were considered in previous computational calculations for the pure monoclinic $\mathrm{ZrO_2}$

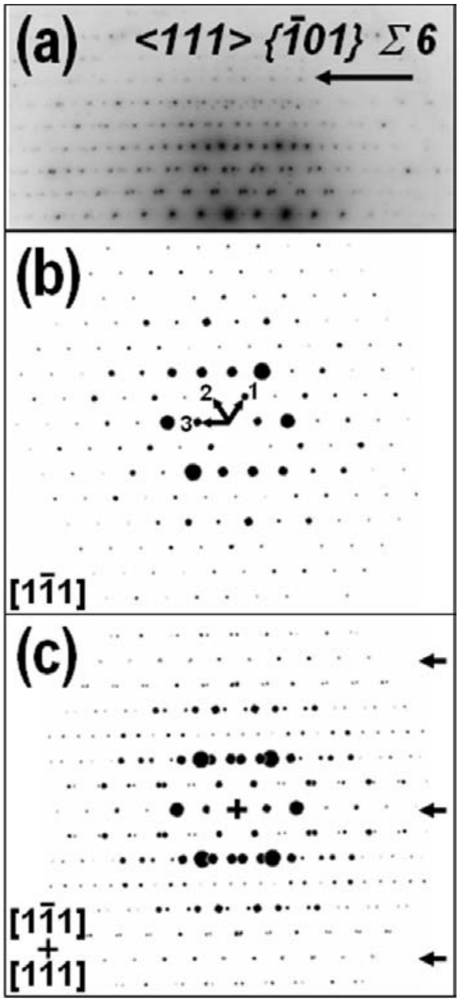

Figure 7
Diffraction associated with a ⟨111⟩ {$\bar{1}$01} Σ6 twin in an La-containing monoclinic grain. (*a*) Experimental SAED pattern; (*b*) calculated diffraction pattern for a single lath being 1, 2 and 3 of the 110, 011 and $\bar{1}$01 m-$\mathrm{ZrO_2}$ reflections, respectively. (*c*) The calculated diffraction for both crystals demonstrates the Σ6 CSL index of the GB.

Table 1
Specific twin junctions in different monoclinic grains of the doped ZrO_2 systems.

(*1) indicates that the (001) monoclinic planes have continuity with the (010) planes of the adjacent [001] *m*-grain; (*2) indicates *m*-(001) continuity with (010) of the adjacent [101] *t*-grain. Note the following equivalences for the monoclinic system: {110}: $(110) = (\bar{1}10) = (1\bar{1}0) = (\bar{1}\bar{1}0)$; {001}: (001); $\{\bar{1}01\}$: $(\bar{1}01) = (10\bar{1})$; {100}: $(100) = (\bar{1}00)$.

Sample	Zone axis	Twin (*n*-CSL)
Sc-doped ZrO_2	⟨010⟩	(001) $\Sigma3$ *1
	⟨110⟩	{110} $\Sigma6$
	⟨011⟩	{100} $\Sigma3$
Y-doped ZrO_2	⟨011⟩	{100} $\Sigma3$ *2
	⟨111⟩	{110} $\Sigma7$
Nd-doped ZrO_2	⟨011⟩	{100} $\Sigma3$
Yb-doped ZrO_2	⟨010⟩	(001) $\Sigma3$ *1
La-doped ZrO_2	⟨111⟩	$\{\bar{1}\,01\}$ $\Sigma6$

(Gertsman *et al.*, 1996), where $\Sigma6$ junctions with different twin planes than those reported here were also proposed. However, $\Sigma7$ twins are not expected solutions. In contrast, when the contact plane is {110} or {001} (as with those observed in our $\Sigma6$ and $\Sigma7$ twins), two different types of $\Sigma71$ CSL twins would be expected by the commented computational calculations. There might be some correspondence between these two proposed types of CSL twin if different criteria are used for the network-matching requirements. In addition, $\Sigma3$ and $\Sigma71$ twins were found in one experimentally different system: thin ZrO_2 corrosion films (Gertsman, 1999; Gertsman *et al.*, 1999). Moreover, taking into account that:

(i) low-symmetry lattices have multiple twin variants,

(ii) low Σ values have particularly small grain-boundary energies and

(iii) the CSL could be influenced by small differences in the dopant composition between two attached twinned domains, multiple solutions are feasible. In this way, dopant cations might enhance one or more stable low-energy CSL configurations since their presence in the ZrO_2 network slightly influences the atomic positions and mechanisms of phase transformations (Yoshimura *et al.*, 1990; Benyagoub, 2005).

As a conclusion, the characterization of various twin boundaries has been carried out by the analysis of electron diffraction patterns registered when the electron beam was parallel to the twin plane. The observed low values in the *n*-CSL character of the resulting junctions ($\Sigma3$, $\Sigma6$ or $\Sigma7$) indicate that special grain boundaries of expected low energy are often present in monoclinic ZrO_2 doped with trivalent cations of the rare-earth elements.

This research has been supported by a program of international collaboration between the European Commission (GDR-200–30211) and the American National Science Foundation (DMR-0099695). FMM thanks the Max Planck Society and the Alexander von Humboldt Foundation for the financial support. C. G. Levi, V. Gertsman and M. Hopkinson are also acknowledged for their fruitful discussions.

References

Atkinson, A., Barnett, S., Gorte, R. J., Irvine, J. T. S., McEvoy, A. J., Mogensen, M., Singhal, S. C. & Vohs, J. (2004). *Nature Mater.* **3**, 17–27.

Benyagoub, A. (2005). *Phys. Rev. B*, **72**, 094114:1–7.

Bhattacharya, K., Conti, S., Zanzotto, G. & Zimmer, J. (2004). *Nature*, **428**, 55–59.

Bocanegra-Bernal, M. H. & De la Torre, S. D. (2002). *J. Mater. Sci.* **37**, 4947–4971.

Gertsman, V. Y. (1999). *Interface Sci.* **7**, 231–242.

Gertsman, V. Y., Lin, Y. P., Zhilayev, A. P. & Szpunar, J. (1999). *Philos. Mag. A*, **79**, 1567–1590.

Gertsman, V. Y., Zhilayev, A. P. & Szpunar, J. (1996). *Scr. Mater.* **35**, 1247–1251.

Gertsman, V. Y., Zhilyaev, A. P. & Szpunar, J. A. (1997). *Modell. Simul. Mater. Sci. Eng.* **5**, 35–52.

Grimmer, H. (1976). *Acta Cryst.* A**32**, 783–785.

Javey, A., Kim, H., Brink, M., Wang, Q., Ural, A., Guo, J., McIntyre, P., McEuen, P., Lundstrom, M. & Dai, H. (2002). *Nature Mater.* **1**, 241–246.

Kim, C. S., Rollet, A. D. & Rohrer, G. S. (2006). *Scr. Mater.* **54**, 1005–1009.

Lanteri, V., Heuer, A. H. & Mitchel, T. E. (1984). *Science and Technology of Zirconia II*, edited by A. H. Heuer, N. Claussen & M. Rühle, Vol. 12, pp. 118–130. American Ceramic Society, Columbus, Ohio.

Levi, C. G. (2004). *Mater. Sci.* **8**, 77–91.

Morales, F. M., Rebollo, N., Wang, C., Zinkevich, M., Aldinger, F., Levi, C. G. & Rühle M. (2006). In preparation.

Rebollo, N. R., Ghandi, A. S. & Levi, C. G. (2003). *Electrochemical Society Proceedings*, edited by E. J. Opila, P. Hou, T. Maruyama, B. Pieraggi, M. McNallan, D. Shifler & E. Wuchima, Vol. PV2003-16, pp. 431–442. Pennington, NJ: Electrochemical Society Inc.

Rohrer, G. S., Saylor, D. M., El Dasher, B., Adams, B. L., Rollet, A. D. & Wynblatt, P. (2004). *Z. Metallkdd.* **95**, 197–214.

Simha, N. K. (1997). *J. Mech. Phys. Solids*, **45**, 261–292.

Subbaro, E. C. (1981). *Advances in Ceramics: Science and Technology of Zirconia*, edited by A. H. Heuer & L. W. Hobbs, Vol. 3, pp. 1–24. American Ceramic Society, Columbus, Ohio.

Torsello, G., Lomascolo, M., Licciulli, A., Diso, D., Tundo, S. & Mazzer M. (2004). *Nature Mater.* **3**, 632–637.

Watanabe, T. (1994). *Mater. Sci. Eng. A*, **176**, 39–49.

Williams, D. B. & Carter, C. B. (1996). *Transmission Electron Microscopy: A Textbook for Materials Science*, Vol. 416, p. 416. New York: Kluwer Academic, Plenum Publishers.

Yoshimura, M., Yashima, M., Noma, T. & Somoya, S. (1990). *J. Mater. Sci.* **25**, 2011–2016.

Zhang, Y. L., Jin, X. J., Rong, Y. H., Hsu, T. Y., Jiang, D. Y. & Shi, J. L. (2006). *Acta Mater.* **54**, 1289–1295.

Zinkevich, M., Wang, Ch., Morales, F. M., Rühle, M. & Aldinger, F. (2005). *J. Alloy Compd*, **398**, 261–268.